Mon. Not. R. Astron. Soc. **418,** 2207–2218 (2011) doi:10.1111/j.1365-2966.2011.19474.x

The ISW–tSZ cross-correlation: integrated Sachs–Wolfe extraction out of pure cosmic microwave background data

N. Taburet,[1⋆] C. Hernández-Monteagudo,[2,3] N. Aghanim,[1] M. Douspis[1] and R. A. Sunyaev[2,4]

[1]*Institut d'Astrophysique Spatiale, Université Paris-Sud 11 & CNRS (UMR 8617), Bât. 121, 91405 Orsay Cedex, France*
[2]*Max-Planck-Institut für Astrophysik, Karl-Schwarzschild-Str. 1, 85740 Garching, Germany*
[3]*Centro de Estudios de Física del Cosmos de Aragón (CEFCA), Plaza San Juan, 1, Planta 2, E-44001 Teruel, Spain*
[4]*Space Research Institute, Russian Academy of Sciences, Profsoyuznaya 84/32, 117997 Moscow, Russia*

Accepted 2011 July 19. Received 2011 July 19; in original form 2010 November 26

ABSTRACT

If dark energy introduces an acceleration in the universal expansion then large-scale gravitational potential wells should be shrinking, causing a blueshift in the cosmic microwave background (CMB) photons that cross such structures [integrated Sachs–Wolfe (ISW) effect]. Galaxy clusters are known to probe those potential wells. In these objects, CMB photons also experience inverse Compton scattering off the hot electrons of the intracluster medium and this results in a distortion with a characteristic spectral signature of the CMB spectrum [the so-called thermal Sunyaev–Zel'dovich (tSZ) effect]. Since both the ISW and the tSZ effects take place in the same potential wells, they must be spatially correlated. We present how this cross-ISW–tSZ signal can be detected in a CMB data contained way by using the frequency dependence of the tSZ effect in multifrequency CMB experiments like *Planck*, *without* requiring the use of external large-scale structure tracers data. We find that by masking low-redshift clusters, the shot noise level decreases significantly, boosting the signal-to-noise ratio of the ISW–tSZ cross-correlation. Nevertheless, in a more realistic case in which we only mask the clusters that could be detected by *Planck*, detection of the ISW–tSZ cross-signal is expected to reach only low significance (1.5σ) unless external cluster catalogues are used to mask the tSZ signal coming from lower mass clusters at low z that do not significantly contribute to the signal but to the shot noise. We also find that galactic and extragalactic dust residuals must be kept at or below the level of $\sim$0.04 $(\mu\mathrm{K})^2$ at $\ell = 10$, a limit that is a factor of a few below *Planck*'s expectations for foreground subtraction. If this is achieved, CMB observations of the ISW–tSZ cross-correlation should also provide an independent probe for the existence of dark energy and the amplitude of density perturbations.

Key words: methods: statistical – galaxies: clusters: general – cosmic background radiation – cosmology: theory.

1 INTRODUCTION

The primary cosmic microwave background (CMB) and especially its angular power spectrum provides us with powerful constraints on the content of the Universe and its evolution. It is now well established that an accurate understanding of the primary CMB power spectrum requires a good comprehension of the secondary CMB anisotropies resulting from the interaction of the CMB photons with the matter along the line of sight from the last scattering surface to the observer (see Aghanim, Majumdar & Silk 2008, for a review). The great efforts undertaken to understand these secondary anisotropies, in order to best recover the primary CMB, also provide us with powerful independent cosmological probes when the secondary anisotropies are regarded as a source of information rather than contamination.

Among those secondary CMB anisotropies, some result from the gravitational interaction of the CMB photons with the potential wells they cross. One of them is the integrated Sachs–Wolfe (ISW) effect, by which CMB photons experience some blue/redshift as they pass through large-scale time-evolving potential wells (Sachs & Wolfe 1967). Since a dark energy like component is expected to affect the growth of large-scale structures (LSSs), making them shallower, a detection of the ISW effect is an important probe for establishing its existence – provided that the Universe is flat and

⋆E-mail: nicolas.taburet@ias.u-psud.fr

general relativity is a correct description of gravity – and constraining the equation of state of such a component.

Detection claims of the ISW effect arose as soon as the first-year *Wilkinson Microwave Anisotropy Probe* (*WMAP*) data were released. Those claims were based upon cross-correlation analyses of *WMAP* CMB data and galaxy density templates built from different surveys. While most of the first analyses were conducted in real space (i.e. by computing the angular cross-correlation function), subsequently new results based upon Fourier/multipole and wavelet space were presented. The results from the *WMAP* team on the cross-correlation of National Radio Astronomy Observatory (NRAO) Very Large Sky Survey (NVSS) with *WMAP* data (Nolta et al. 2004) were soon followed by other analyses applied not only on NVSS data, but also on X-ray and optical based catalogues like the *High Energy Astronomy Observatory (HEAO)*, Sloan Digital Sky Survey (SDSS), Automatic Plate Measuring machine (APM) or Two Micron All Sky Survey (2MASS) (Fosalba, Gaztañaga & Castander 2003; Scranton et al. 2003; Afshordi, Loh & Strauss 2004; Boughn & Crittenden 2004; Fosalba & Gaztañaga 2004). As subsequent data releases from both the CMB and the SDSS side became public, new studies prompted further evidence for significant cross-correlation between CMB and LSS data (e.g. Padmanabhan et al. 2005; Cabré et al. 2006; Giannantonio et al. 2006; Rassat, Land & Lahav 2007). By that time, wavelet techniques were also applied on NVSS and *WMAP* data, providing the highest significance ISW detection claims at the level of 3σ–4σ (Pietrobon, Balbi & Marinucci 2006; Vielva, Martínez-González & Tucci 2006; McEwen et al. 2007). The initial effort of Granett, Neyrinck & Szapudi (2008), consisting in stacking voids and superclusters extracted from SDSS data, yielded a very high significance ($\sim 4\sigma$) ISW detection claim. However, it was later found in Granett, Neyrinck & Szapudi (2009) that such signal could not be due to ISW only, since a gravitational potential reconstruction from the luminous red galaxy (LRG) sample of SDSS yielded a much lower signal ($\sim 2.5\sigma$). Giannantonio et al. (2008) and Ho et al. (2008) used different LSS surveys in a combined cross-correlation analysis with CMB data and claimed high significance ($\sim 4\sigma$–5σ) ISW detections.

However, doubts on the validity of such claims have also arisen recently. Hernández-Monteagudo, Génova-Santos & Atrio-Barandela (2006a) first pointed out the lack of significant cross-correlation between *WMAP* first-year data and density surveys built upon 2MASS, SDSS and NVSS on the large angular scales, but detected the presence of radio point-source emission and thermal Sunyaev–Zel'dovich (tSZ) effect on the small scales. In Hernández-Monteagudo (2008) a study of the expected signal-to-noise ratio (S/N) for different sky coverages was presented, and it was found that in the standard Λ cold dark matter (ΛCDM) scenario the ISW–density cross-correlation should be well contained in the largest angular scales ($l < 50$–60). This was proposed as a consistency check for ISW detection against point-source contamination. In Hernandez-Monteagudo (2010) cross-correlation analyses between NVSS and *WMAP* fifth-year data provided no evidence for cross-correlation in the large angular range ($l < 60$). A signal at the 2σ–3σ level was however found at smaller scales, although its significance increased with increasing flux thresholds applied on NVSS sources (in contradiction with expectations for the ISW probed by NVSS and raising the issue of radio point-source contamination). Furthermore, the intrinsic clustering of NVSS sources on the large scales (relevant for the ISW) was found too high for the commonly assumed redshift distribution for NVSS sources, as found in previous works (Negrello, Magliocchetti & De Zotti 2006; Raccanelli et al. 2008). Regarding ISW detection claims based upon SDSS data, there is also some ongoing discussion after recent failures in finding any statistical significance for the ISW (Bielby et al. 2010; López-Corredoira, Sylos Labini & Betancort-Rijo 2010; Sawangwit et al. 2010). This situation is partially caused by the fact that the ISW is generated on the large angular scales and at moderate to high redshifts ($z \in [0.1, 1.3]$). Deep galaxy surveys covering large fractions of the sky are hence required to sample the ISW properly, but those are not available yet (or not properly understood).

Ideally one would try to find the ISW contribution to CMB anisotropies by using CMB data *exclusively*. Moreover, in this context the tSZ effect becomes of relevance. The tSZ effect (Sunyaev & Zel'dovich 1972) results from the inverse Compton scattering of the CMB photons off the galaxy cluster electrons, and is expected to provide cosmological constraints on the normalization at $8\,h^{-1}$ Mpc of the density fluctuations power spectrum, σ_8, as well as on the amount of matter $\Omega_{\rm m}$ and to a lower extent on the dark energy equation of state (e.g. Battye & Weller 2003). Since both the tSZ and the ISW effects probe LSSs and their evolution, a correlation is therefore expected between these two signals. As Hernández-Monteagudo & Sunyaev (2005) pointed out, provided that the tSZ has a definite and well-known frequency dependence, it is possible to combine different CMB maps obtained at different frequencies in search for a *frequency-dependent* ISW–tSZ cross-correlation. The advantages of this approach are twofolded: (i) only CMB data (obtained at different frequency channels) are required, and hence there is no need for using and characterizing an external LSS catalogue and (ii) a better handle on systematics is provided since the ISW–tSZ cross-correlation has a perfectly known frequency dependence that can be searched for in multiple channel combinations. This approach in experiments like *Planck*,[1] covering the whole sky in a wide frequency range, is well suited to separate the tSZ from other components present in the microwave range.

The CMB and tSZ maps correlation had already been considered by Cooray (2002) who pointed out that the tSZ one-halo term, which constitutes most of the tSZ signal, does not trace LSS correlations and therefore limits the ISW–tSZ possible level of detectability. In this paper, we propose an original method to reduce this contamination and quantify its limitations.

After introducing in Section 2 the theoretical background, we study in Section 3 a combination of CMB maps at different frequencies that provide an unbiased estimate of the ISW–tSZ angular power spectrum. We also compute the expected significance for the ISW–tSZ cross-correlation. In Section 4 we analyse how the LSS contributes to the tSZ and ISW autopower spectra in different redshift ranges. This allows us to define a strategy to optimize the S/N of the ISW–tSZ cross-correlation by applying a selective mask on galaxy clusters. We then investigate in Section 5 the limitations of our method due to the presence of galactic and extragalactic foregrounds and suggest some approaches to minimize their impact. We present our conclusions in Section 6.

2 ANGULAR POWER SPECTRA OF LARGE SCALE STRUCTURE TRACERS

CMB photons can interact with the matter situated along the line of sight from the last scattering surface to the observer, and thus suffer gravitational or scattering effects. This produces fluctuations in the observed CMB temperature on the sky. The most important scattering effect is known as the Sunyaev–Zel'dovich (SZ) effect

[1] http://www.sciops.esa.int/index.php?project=PLANCK.

that arises when CMB photons scatter off the electrons of the intracluster gas. Since these electrons are lying within the LSS potential wells, a correlation is thus expected between the SZ effect and the ISW temperature fluctuations due to the energy change of the CMB photons that pass through time evolving potential wells.

2.1 Late ISW

In a ΛCDM scenario, the accelerated expansion of the universe makes large-scale potential wells to shrink. As a consequence, CMB photons crossing a potential well ϕ do not lose as much energy exiting this well as what they gained when falling into it. This is known as the late ISW effect and results in a modification of the CMB blackbody temperature (e.g. Martinez-Gonzalez, Sanz & Silk 1990):

$$\frac{\Delta T}{T_{\rm CMB}} = -\frac{2}{c^2}\int \mathrm{d}\eta \frac{\mathrm{d}\phi}{\mathrm{d}\eta}, \tag{1}$$

where η is the conformal time defined as $\mathrm{d}\eta = \mathrm{d}t/a(t)$, where t and $a(t)$ are the coordinate time and the scalefactor in a standard Friedmann–Robertson–Walker metric. The relation between the gravitational potential and matter distribution variations is given by the Poisson equation in physical coordinates:

$$\nabla^2\phi = 4\pi G\bar{\rho}_{\rm m}(1+\delta). \tag{2}$$

This equation is easier to solve in the comoving frame and in Fourier space (k stands for the wavenumber and the subscript c denotes comoving units):

$$\phi(k) = -\frac{3}{2}H_0^2\Omega_{\rm m0}\frac{\delta_{k_{\rm c}}}{ak_{\rm c}^2}, \tag{3}$$

where H_0 is the Hubble constant. We have used the relation between the critical density of the Universe and the expansion rate of the homogeneous background $\rho_{\rm c}(a) = [3H^2(a)]/(8\pi G) = \rho_{\rm m}(a)/[\Omega_{\rm m0}a^{-3}(\frac{H_0}{H(a)})^2]$.

In the linear regime, as long as the different k modes are not coupled to each other, the matter overdensity for a pressureless fluid can be written as $\delta_k(a) = D_+(a)\delta_k(z=0)$ where the growing mode $D_+(a)$ is a solution to the following differential equation:

$$\ddot{\delta}(k) + 2H\dot{\delta}(k) = 4\pi G\bar{\rho}_{\rm m}\delta(k), \tag{4}$$

in which dots denote a derivation with respect to the physical time.

Using equation (3) we can express the CMB temperature fluctuations due to the ISW in the linear regime:

$$\frac{\Delta T}{T_{\rm CMB}} = \frac{3H_0^2}{c^2}\Omega_{\rm m0}\int \frac{a\,\mathrm{d}\boldsymbol{r}_{\rm c}}{c}\frac{\mathrm{d}}{\mathrm{d}t}\left(\frac{D_+(a)}{a}\right)\int\frac{\mathrm{d}^3\boldsymbol{k}_{\rm c}}{(2\pi)^3}\frac{\delta_{k,z=0}}{k_{\rm c}^2}\mathrm{e}^{-\mathrm{i}\boldsymbol{k}_{\rm c}\cdot\boldsymbol{r}_{\rm c}}. \tag{5}$$

The temperature fluctuations due to the ISW effect can be projected on the spherical harmonics basis,

$$a_{\ell m}^{\rm ISW} = 4\pi(-\mathrm{i})^\ell\int\frac{\mathrm{d}^3\boldsymbol{k}_{\rm c}}{(2\pi)^3}Y_{\ell m}^*(\boldsymbol{k}_{\rm c})\Delta_\ell^{\rm ISW}(k_{\rm c})\delta_{k_{\rm c},z=0}, \tag{6}$$

with the ISW transfer function:

$$\Delta_\ell^{\rm ISW}(k_{\rm c}) = \frac{3H_0^2}{c^3}\Omega_{\rm m0}\int \mathrm{d}r_{\rm c}a\frac{\mathrm{d}}{\mathrm{d}t}\left(\frac{D_+(a)}{a}\right)\frac{1}{k_{\rm c}^2}j_\ell(k_{\rm c}r_{\rm c}). \tag{7}$$

2.2 The thermal SZ effect

The SZ effect consists of two terms. The main one is the tSZ effect that is due to the inverse Compton scattering of the CMB photons off the intracluster gas hot electrons. The second one is the kinetic SZ effect (kSZ) which is a Doppler shift due to galaxy clusters' motion with respect to the CMB rest frame. The tSZ effect transfers some energy from the hot electrons to the CMB photons. As a result, in the direction of the cluster, the CMB intensity is decreased in the Rayleigh–Jeans part of the spectrum and increased in the Wien part. This translates into a characteristic spectral signature g_ν of the induced CMB temperature secondary fluctuations, expressed as a function of the adimensional frequency $x = h\nu/(k_{\rm B}T_{\rm e})$ and the Comptonization parameter y. Neglecting relativistic corrections, this parameter can be written as

$$\frac{\Delta T}{T_{\rm CMB}} = g_\nu y = \left(x\frac{\mathrm{e}^x+1}{\mathrm{e}^x-1} - 4\right)y. \tag{8}$$

The Comptonization parameter y corresponds to the integrated electronic pressure along a given line of sight through the cluster:

$$y = \frac{k_{\rm B}\sigma_{\rm T}}{m_{\rm e}c^2}\int \mathrm{d}l\, n_{\rm e}T_{\rm e}. \tag{9}$$

The kSZ, on the other hand, does not have a different spectral signature from the CMB. The secondary temperature fluctuations power spectrum due to the kSZ is about two to four times smaller than the one induced by the tSZ at 150 GHz (Lueker et al. 2010; Sehgal et al. 2010). We can safely neglect its contribution in our analysis as explained in Section 3.

In order to calculate the temperature fluctuations due to a population of N clusters, one can use the halo approach (Cole & Kaiser 1988; Cooray & Sheth 2002). In this paper, we adopt the line-of-sight approach that was introduced in Hernández-Monteagudo et al. (2006b):

$$\frac{\Delta T}{T_{\rm CMB}} = g_\nu\int \mathrm{d}\boldsymbol{r}_{\rm p}\sum_i^N y_{\rm 3D,c}(r_{\rm p})u(\boldsymbol{r}_{\rm p}-\boldsymbol{w}_i) \tag{10}$$

where $r_{\rm p}$ stands for physical distances, $\boldsymbol{w}$ for the line-of-sight position and $y_{\rm 3D,c}$ is the value of $\frac{k_{\rm B}T_{\rm e}}{m_{\rm e}c^2}\sigma_{\rm T}n_{\rm e}$ at the centre of the cluster and u is the electronic radial pressure profile, $y_{\rm 3D}(w) = y_{\rm 3D,c}u(w)$. Replacing the discrete summation with an integral over the position we get

$$\frac{\Delta T}{T_{\rm CMB}} = g_\nu\int \mathrm{d}\boldsymbol{r}_{\rm p}\int \mathrm{d}M y_{\rm 3D,c}(M,r_{\rm p})\int \mathrm{d}\boldsymbol{w}_{\rm p}\left.\frac{\mathrm{d}n}{\mathrm{d}M}\right|_{\rm p}(w_{\rm p},M,r_{\rm p}) \times u(\boldsymbol{r}_{\rm p}-\boldsymbol{w}_{\rm p},M,r_{\rm p}). \tag{11}$$

The convolution between the mass function and the cluster profile is easier to handle in Fourier space:

$$\frac{\Delta T}{T_{\rm CMB}} = g_\nu\int \mathrm{d}\boldsymbol{r}_{\rm p}\int \mathrm{d}M\int\frac{\mathrm{d}^3\boldsymbol{k}_{\rm p}}{(2\pi)^3}\left.\frac{\mathrm{d}n}{\mathrm{d}M}\right|_{\rm p}(k_{\rm p},M,r_{\rm p}) \times\tilde{y}_{\rm 3D}(k_{\rm p},M,r_{\rm p})\mathrm{e}^{-\mathrm{i}\boldsymbol{k}_{\rm p}\cdot\boldsymbol{r}_{\rm p}}. \tag{12}$$

Since galaxy clusters are not exclusively Poisson distributed, in the Fourier description of the spatial distribution of these sources a correlation term is added to the Poisson term. It represents the modulation of the cluster number density by the underlying density field:

$$\left.\frac{\mathrm{d}n}{\mathrm{d}M}\right|_{\rm p}(\boldsymbol{k}_{\rm p},M,r_{\rm p}) = \left.\frac{\mathrm{d}\bar{n}}{\mathrm{d}M}\right|_{\rm p}(M,r_{\rm p})\left[\delta_{\rm D}(\boldsymbol{k}_{\rm p}) + b(M,r_{\rm p})\delta_k\right], \tag{13}$$

where the linear bias is modelled with $b(M,z) = 1 - 1/\delta_{\rm c} + \delta_{\rm c}/\sigma^2(R,z)$ (Mo & White 1996).

That is, the power spectrum of the tSZ angular anisotropy can be written as the contribution of two different terms (e.g. Komatsu & Kitayama 1999). The first one refers to the Poisson/discrete nature of these sources, and is known as the one-halo term. The second one

refers to the spatial modulation of the density of these sources, obeying the large-scale density field, and is referred to as the two-halo term, which is sensitive to the underlying matter density distribution. In this paper, we are mainly interested in the detection of the cross-ISW–tSZ term, to which only this second term contributes.

The temperature fluctuations due to the SZ effect two-halo term can be projected on the spherical harmonics basis,

$$a_{\ell m}^{\rm tSZ2h} = 4\pi(-{\rm i})^{\ell} \int \frac{{\rm d}^3 k_{\rm p}}{(2\pi)^3} Y^*_{\ell m}(\boldsymbol{k}_{\rm p}) \Delta_{\ell}^{\rm tSZ2h}(k_{\rm p}) \delta_{k_{\rm p},z=0} \tag{14}$$

with the tSZ two-halo term transfer function:

$$\Delta_{\ell}^{\rm tSZ2h}(k_{\rm p}) = g_{\nu} \int {\rm d}r_{\rm p} \int {\rm d}M \left.\frac{{\rm d}\bar{n}}{{\rm d}M}\right|_{\rm p} (M, r_{\rm p}) b(M, r_{\rm p}) \times \tilde{y}_{\rm 3D}(k_{\rm p}, M, r_{\rm p}) D_+(r_{\rm p}) j_{\ell}(k_{\rm p} r_{\rm p}). \tag{15}$$

The Fourier transform of $y_{\rm 3D}(r)$ is

$$\tilde{y}_{\rm 3D}(k_{\rm p}, M, z) = 4\pi \int y_{\rm 3D}(r_{\rm p}, M, z) j_0(k_{\rm p} r_{\rm p}) r_{\rm p}^2 \, {\rm d}r_{\rm p}. \tag{16}$$

Switching to comoving units, we write the $a_{\ell m}$ in a form similar to equations (6) and (7):

$$a_{\ell m}^{\rm tSZ2h} = 4\pi(-{\rm i})^{\ell} \int \frac{{\rm d}^3 k_{\rm c}}{(2\pi)^3} Y^*_{\ell m}(\boldsymbol{k}_{\rm c}) \Delta_{\ell}^{\rm tSZ2h}(k_{\rm c}) \delta_{k_{\rm c},z=0} \tag{17}$$

with the tSZ two-halo term transfer function:

$$\Delta_{\ell}^{\rm tSZ2h}(k_{\rm c}) = g_{\nu} \int a \, {\rm d}r_{\rm c} \int {\rm d}M a^{-3} \left.\frac{{\rm d}\bar{n}}{{\rm d}M}\right|_{\rm c} (M, r_{\rm c}) b(M, r_{\rm c}) \times \tilde{y}_{\rm 3D}(k_{\rm p}, M, r_{\rm c}) D_+(r_{\rm c}) j_{\ell}(k_{\rm c} r_{\rm c}). \tag{18}$$

In the following, we have used the Sheth, Mo & Tormen (2001) mass function, the Komatsu & Seljak (2002, hereafter KS02) model for the intracluster electronic distribution and the *WMAP* fifth-year cosmological parameters (Komatsu et al. 2009): $\Omega_{\Lambda} = 0.721$, $\Omega_{\rm m} = 0.279$, $\Omega_{\rm b} = 0.046$, $h = 0.701$, $\sigma_8 = 0.817$ and $n_{\rm s} = 0.96$.

2.3 ISW–tSZ cross-power spectrum

Using equations (6), (7), (17) and (18) it is straightforward to obtain the cross-correlation between the ISW effect and the tSZ effect:

$$C_{\ell}^{\rm ISW-tSZ} = \left\langle a_{\ell m}^{\rm ISW} a_{\ell m}^{\rm tSZ2h *} \right\rangle = \frac{2}{\pi} \int k_{\rm c}^2 {\rm d}k_{\rm c} \Delta_{\ell}^{\rm ISW}(k_{\rm c}) \Delta_{\ell}^{\rm tSZ2h}(k_{\rm c}) P(k_{\rm c}, z=0), \tag{19}$$

where we have introduced the matter power spectrum:

$$\left\langle \delta_{\boldsymbol{k},z=0} \delta^*_{\boldsymbol{k}',z=0} \right\rangle = (2\pi)^3 \delta_{\rm D}(\boldsymbol{k} - \boldsymbol{k}') P(k, z=0). \tag{20}$$

We speed up the computation of the power spectra by adopting the Limber approximation:

$$C_{\ell}^{\rm ISW-tSZ} \simeq g_{\nu} \frac{3H_0^2}{c^3} \Omega_{\rm m0} \int {\rm d}z \frac{1}{4\pi} \frac{{\rm d}V_{\rm c}}{{\rm d}z} P_{\rm m}\left(\frac{\ell+1/2}{D_{\rm c}}, z=0\right) \times \left(\frac{1}{\ell+1/2}\right)^2 a \frac{\partial}{\partial t}\left(\frac{D_+(a)}{a}\right) D_+(a) \int {\rm d}M \left.\frac{{\rm d}\bar{n}}{{\rm d}M}\right|_{\rm c} (M, z) \times b(M, z) \tilde{y}_{\rm 3D}\left(\frac{\ell+1/2}{D_{\rm A}}, M, z\right). \tag{21}$$

This Limber approximation is based on the closing relation of the spherical Bessel function,

$$\int k^2 {\rm d}k j_{\ell}(kr_1) j_{\ell}(kr_2) \mathcal{F}(k) \simeq \frac{\pi}{2} \frac{\delta_{\rm D}(r_2 - r_1)}{r_1^2} \mathcal{F}\left(\frac{\ell+1/2}{r_1}\right), \tag{22}$$

where $\mathcal{F}$ is a function that slowly varies with k. We used $k = \frac{\ell+1/2}{r}$ in order to ensure an error in $\mathcal{O}(\ell^{-2})$ while the frequently employed flat sky approximation $k = \ell/r$ only ensures an error in $\mathcal{O}(\ell^{-1})$ (Loverde & Afshordi 2008).

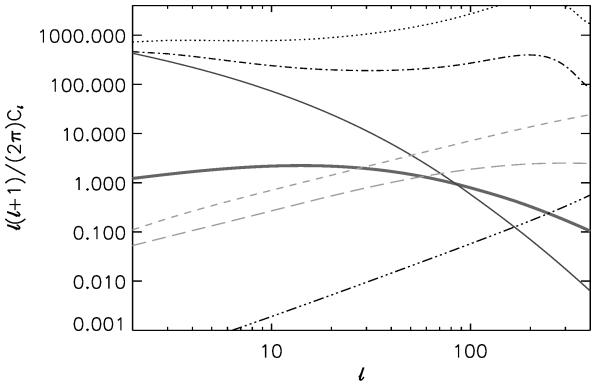

Figure 1. ISW–tSZ angular cross-power spectrum at 100 GHz (thick solid red line), ISW angular power spectrum (thin solid blue), tSZ one-halo term (short-dashed green), tSZ two-halo term (long-dashed green). The CMB power spectrum is represented as a black dotted line for comparison. The dot–dashed line represents the cosmic variance associated to the CMB and the triple-dot–dashed line is the *Planck* noise at 100 GHz.

In Fig. 1, we present the CMB–CMB, ISW–ISW, tSZ–tSZ and ISW–tSZ power spectra calculated at 100 GHz without using the Limber approximation. We also represent the instrumental noise for a *Planck* like experiment as well as the cosmic variance associated to the CMB.

Fig. 2 represents the relative difference between the various angular power spectra calculated using the Limber or the exact formula. While the 'standard' Limber approximation ($k \simeq \ell/r$) ensures a 10 per cent precision from $\ell \geq 6$ and $\ell \geq 20$ for the tSZ–tSZ and ISW–ISW power spectra, respectively, these limit multipoles become $\ell \geq 3$ and $\ell \geq 1$ when using the $k \simeq (\ell + 1/2)/r$ approximation. As discussed in Afshordi et al. (2004) the errors induced by this later approximation are small compared to the cosmic variance. Therefore, in the following we use this $k \simeq (\ell + 1/2)/r$ version of the Limber approximation.

The relative amplitude of the ISW–tSZ power spectrum with respect to the contaminant spectra (primary CMB and tSZ) makes it

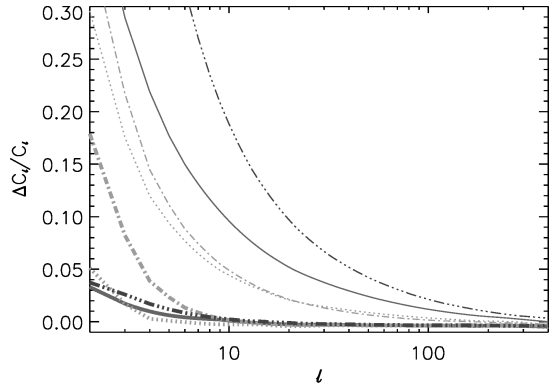

Figure 2. Relative error when using the $k \simeq (\ell + 1/2)/r$ Limber approximation (thick lines) or the $k \simeq \ell/r$ Limber approximation (thin lines). The solid red line stands for the ISW–tSZ angular cross-power spectrum, the triple-dot–dashed blue line for the ISW angular power spectrum, the dot–dashed green line for the tSZ one-halo term and the dotted green line for the tSZ two-halo term. This plot clearly illustrates the great advantage of using the $k \simeq (\ell + 1/2)/r$ approximation instead of the 'standard' $k \simeq \ell/r$ Limber approximation in low ℓ studies of the power spectra.

less difficult to be detected at larger scales than at smaller scales (more details in Section 3, see also Cooray 2002; Hernández-Monteagudo & Sunyaev 2005). For multipoles lower than 100, we see in Fig. 1 that the effect of the instrumental noise can be neglected since its power spectrum is more than one order of magnitude lower than the astrophysical signals considered here. It is nevertheless essential to note that the ISW–tSZ signal, we are interested in measuring, is much smaller than the cosmic variance associated to the CMB. In the next section, we present a method, based on Hernández-Monteagudo & Sunyaev (2005), which uses the characteristic spectral signature of the ISW–tSZ signal, to separate it from the CMB.

3 DETECTION LEVEL OF THE ISW–SZ CROSS-CORRELATION – IDEAL CASE

Hernández-Monteagudo & Sunyaev (2005) have shown that using combinations of multifrequency observations of the microwave sky can allow us to avoid the limit due to the cosmic variance and unveil a weak signal whose frequency signature differs from the CMB blackbody law. Following this idea, we propose a combination of different channels in order to unveil the ISW–tSZ signal, in spite of it being dominated by the primary CMB in each channel. Since the tSZ vanishes at 217 GHz (in the non-relativistic assumption), the channel combination $217 * \nu_i - 217 * 217$ (where $*$ stands for the cross-correlation between the signals from two channels and ν_i is a frequency different from 217 GHz) should give an unbiased estimate of the ISW–tSZ$_{\nu_i}$ cross-power spectrum in the limit in which we neglect the contaminants such as point sources or galactic dust.

In a first analysis we calculate the S/N of the ISW–tSZ in the ideal case in which the noise is only constituted of primary CMB and tSZ autocorrelations. The variance of the $C_\ell^{\mathrm{ISW-tSZ}_{\nu_i}}$ is

$$\Delta^2\left(C_\ell^{\mathrm{ISW-tSZ}_{\nu_i}}\right) = \left\langle \left(a_{\ell m}^{217} a_{\ell m}^{\nu_i} - a_{\ell m}^{217} a_{\ell m}^{217}\right)^2 \right\rangle - \left\langle a_{\ell m}^{217} a_{\ell m}^{\nu_i} - a_{\ell m}^{217} a_{\ell m}^{217} \right\rangle^2 \quad (23)$$

which reduces, in the ideal case, to

$$\Delta^2\left(C_\ell^{\mathrm{ISW-tSZ}_{\nu_i}}\right) = \left[C_\ell^{\mathrm{ISW-tSZ}}\right]^2 + \left(C_\ell^{\mathrm{ISW}} + C_\ell^{\mathrm{CMB}} + N_\ell\right)\left(C_\ell^{\mathrm{tSZ2h}} + C_\ell^{\mathrm{tSZ1h}}\right). \quad (24)$$

The kSZ effect has the same spectral dependence as the primary CMB therefore it will be subtracted by the channel combination we propose. Furthermore, the kSZ contribution, at the large scale of interest in this study, is orders of magnitude smaller than the one coming from the primary CMB, it thus does not affect our estimation of the noise term (equation 24).

For a full sky coverage, the number of independent modes is $2\ell + 1$ and can be approximated as $f_{\mathrm{sky}}(2\ell + 1)$ for a partial sky coverage f_{sky}. We therefore write the S/N for the ISW–tSZ cross-correlation at multipole ℓ as

$$\mathrm{S/N}|_\ell = \left[\frac{(2\ell+1) f_{\mathrm{sky}} \left[C_\ell^{\mathrm{ISW-tSZ}}\right]^2}{\left[C_\ell^{\mathrm{ISW-tSZ}}\right]^2 + \left(C_\ell^{\mathrm{ISW}} + C_\ell^{\mathrm{CMB}} + N_\ell\right)\left(C_\ell^{\mathrm{tSZ2h}} + C_\ell^{\mathrm{tSZ1h}}\right)}\right]^{1/2}. \quad (25)$$

The cumulative S/N up to multipole ℓ for a full sky survey is

$$\mathrm{S/N}(\ell) = \left[\sum_{\ell'=2}^{\ell} \frac{(2\ell'+1)\left[C_{\ell'}^{\mathrm{ISW-tSZ}}\right]^2}{\left[C_{\ell'}^{\mathrm{ISW-tSZ}}\right]^2 + \left(C_{\ell'}^{\mathrm{ISW}} + C_{\ell'}^{\mathrm{CMB}} + N_{\ell'}\right)\left(C_{\ell'}^{\mathrm{tSZ2h}} + C_{\ell'}^{\mathrm{tSZ1h}}\right)}\right]^{1/2}. \quad (26)$$

In case of partial sky coverage or sky cuts of the Galaxy, the low multipoles are not independent anymore, one should adopt a conservative approach starting the summation from $\ell_{\mathrm{min}} \simeq \pi/\theta_{\mathrm{sky}}$, θ_{sky} being the survey size in its smallest dimension (Cooray 2002). Note that in the expression above the g_ν^2 factors describing the frequency dependence of the tSZ effect cancel out. This means that in the ideal case the choice of the frequency ν_i does not affect the S/N level of the ISW–tSZ cross-correlation measurement. Nevertheless, as discussed in Section 5, the level of contaminants will depend on the frequency choice which will have an impact on the S/N.

In Fig. 3 we represent the S/N contribution from each multipole when considering a cosmic variance limited full sky experiment. The solid and dotted lines show the results obtained when using equation (19) and the Limber approximation of equation (21), respectively. Most of the contribution to the S/N comes from multipoles ranging from 5 to 30 with a maximum contribution at $\ell = 13$. This multipole range corresponds to the scales in which the ISW–tSZ cross-term is expected to reach its maximum amplitude and more importantly dominates over the tSZ autocorrelation term.

The results for both the no Limber and Limber approximations are presented in Fig. 4. We found that the cumulative S/N is of the order of 2.2, which is about half the S/N found by Cooray (2002). The main difference between the computation of the angular power spectra in his paper and our computation is that we introduced the Komatsu & Seljak (2002) cluster pressure profile (equation 16) when estimating $C_\ell^{\mathrm{ISW-tSZ}}$ and $C_\ell^{\mathrm{tSZ-tSZ}}$. It is not clear from equations (32) and (33) in Cooray (2002) if they account for the cluster pressure profile and what model they use.

As pointed out by recent CMB experiments (Lueker et al. 2010; Dunkley et al. 2011; Komatsu et al. 2011), the measured tSZ power spectrum seems to have a lower amplitude than expected from analytical calculations or simulations. Apart from point-source residual that could fill the tSZ decrement observed at frequencies below 217 GHz, this discrepancy could be explained if the σ_8 value used to compute the cluster abundance in the spectrum modelization is overestimated. Nevertheless, in this case there would be

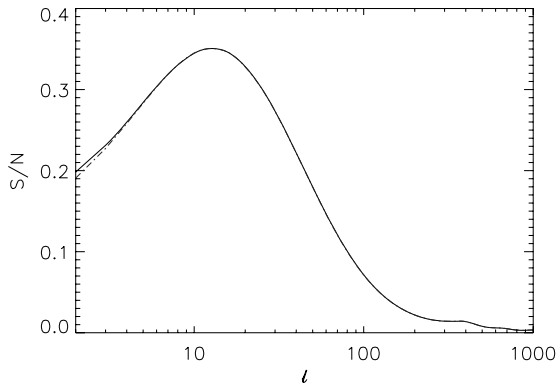

Figure 3. S/N contribution from each multipole for a cosmic variance limited full sky experiment with no contaminants. The solid black is obtained without Limber approximation while the dot–dashed blue line is obtained using the Limber approximation as in equation (21).

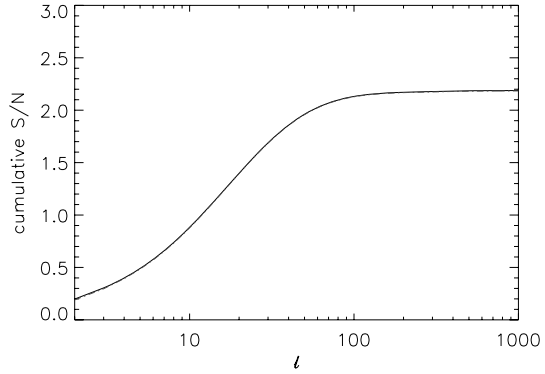

Figure 4. Cumulative S/N, same as Fig. 3.

tension between a lower σ_8 value derived from SZ observations and values derived from primary CMB measurements (Komatsu et al. 2011) or X-ray cluster counts (Vikhlinin et al. 2009). The disagreement between the observed and predicted tSZ power spectrum could also be due to an overestimation of the tSZ effect induced by each individual cluster. Theoretical models describing the electronic density and temperature profiles (such as KS02), output from hydrodynamical numerical simulations (such as those obtained by Sehgal et al. 2010) as well as pressure profiles derived from X-ray observations (such as the one in Arnaud et al. 2010) all seem to predict a higher tSZ power spectrum than what is effectively observed. Physical processes such as supernovae or active galactic nucleus energy feedback to the intracluster medium or a non-thermal pressure contribution could explain the lower level of observed SZ signal (e.g. Shaw et al. 2010). Here we used the theoretical KS02 profile to calculate the power spectra (equation 16). Comparing the effect of various cluster electronic profiles on the amplitude or shape of the ISW–tSZ power spectrum is beyond the scope of this paper and will be investigated in a subsequent work.

The main contribution to the $C_\ell^{\mathrm{ISW-tSZ}}$ variance in equation (24) is the $(C_\ell^{\mathrm{ISW}} + C_\ell{}^{\mathrm{CMB}})(C_\ell^{\mathrm{tSZ2h}} + C_\ell{}^{\mathrm{tSZ1h}})$ term, and especially the tSZ contributions that multiply the CMB noise term. We then propose to mask some SZ clusters in order to significantly reduce the noise term without decreasing too much the ISW–tSZ signal.

4 OPTIMIZING THE ISW–TSZ DETECTION

In order to optimize the detection of the ISW–tSZ signal, we need to determine which clusters contribute more to the ISW–tSZ signal and which clusters are responsible for the tSZ–tSZ shot noise on large scales. We therefore compute the halo contributions to the C_ℓ values, as a function of their redshift, for different ℓ values. We present the results in Fig. 5. On the large scales (several degrees) we are interested in, the tSZ signal mainly comes from clusters at a redshift lower than 0.3 for the two-halo term (dot–dashed red line) and 0.03 for the one-halo term (dashed blue line). On those same angular scales, the ISW signal (dotted green line) mainly arises from time varying potential wells at redshift [0.2; 1]. The cross-ISW–tSZ signal mainly comes from clusters at a redshift $z \in [0.06; 0.8]$ (solid black line). We therefore expect that masking the low redshift clusters will enhance the S/N of the ISW–tSZ.

4.1 Sharp redshift cut

We first apply a sharp cut in redshift in order to simulate the effect of masking low z clusters. The power spectra for a $z = 0.3$ threshold are presented in Fig. 6. As expected, the one-halo term of the tSZ contribution is strongly decreased, as is the two-halo term to a lower extent (solid green lines). For multipoles lower than 100, the dominant tSZ contribution is now the two-halo term. Since the ISW–tSZ signal comes from higher redshift than the tSZ signal, masking has a lower impact on its power spectra. The ISW–ISW signal is only reduced at very large scales ($\ell < 10$) and this relative variation does not exceed 25 per cent.

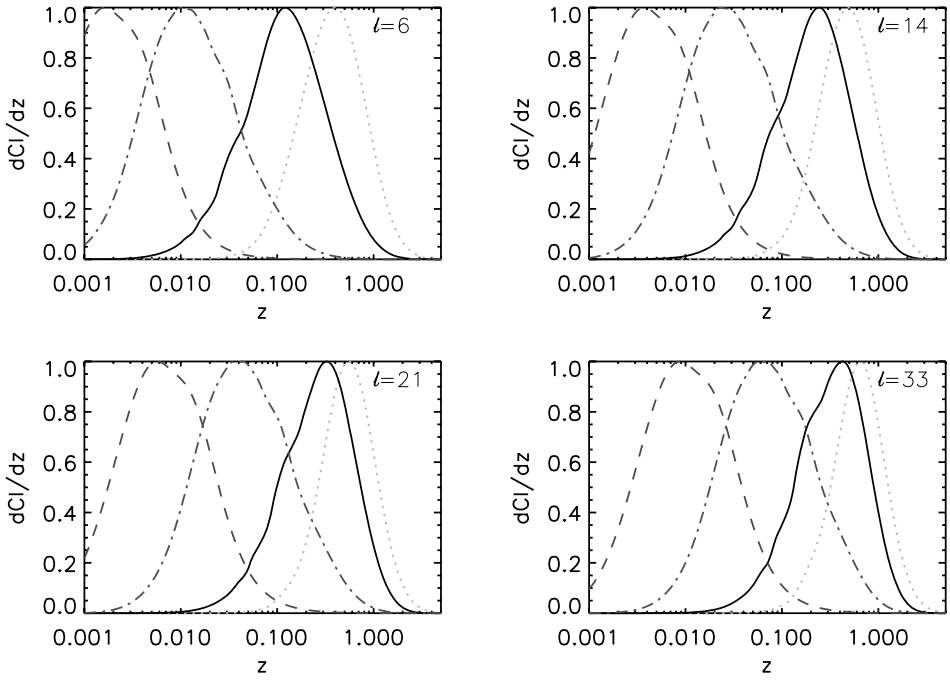

Figure 5. Normalized contribution to the C_ℓ values as a function of the haloes redshift, for different multipoles. The colour coding is as follows: dotted green – ISW–ISW, solid black – ISW–tSZ, dot–dashed red – tSZ–tSZ (two-halo term), dashed blue – tSZ–tSZ (one-halo term).

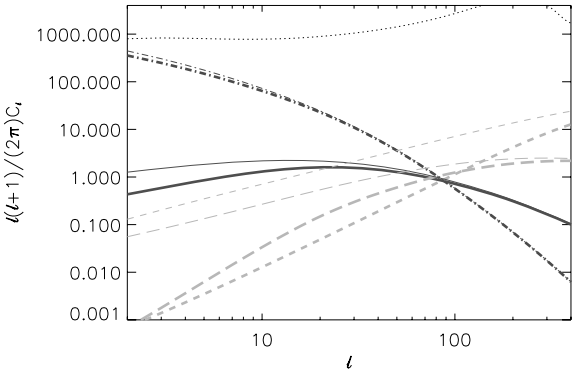

Figure 6. The thick lines represent the power spectra after masking clusters at $z < 0.3$ [The colour coding is as follows: solid red – ISW–tSZ, dot–dashed blue – ISW–ISW, short-dashed green – tSZ–tSZ (one-halo term), long-dashed green – tSZ–tSZ (two-halo term).] For comparison the thin lines represent the contribution due to all clusters. The dotted line is the primary CMB angular power spectrum.

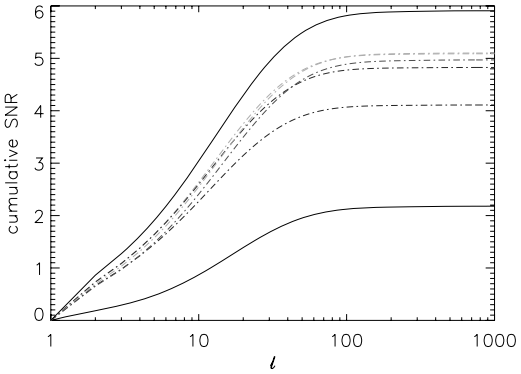

Figure 8. Cumulative S/N of the ISW–tSZ detection in the ideal case ($f_{\rm sky} = 1$, no foregrounds). The dot–dashed curves represent the S/N obtained for different cut in redshift: 0.1 (purple), 0.2 (blue), 0.3 (light blue), 0.4 (green) and 0.5 (red). As a comparison the solid black curve reminds the S/N obtained without masking any cluster. The highest solid black curve is the cumulative S/N obtained for a $z < 0.3$ and $M > 5 \times 10^{14}\,{\rm M}_\odot$ cut.

As shown in Fig. 7, the drastic reduction of the tSZ one-halo term strongly boosts the ISW–tSZ correlation coefficient, which is defined as

$$r_\ell^{\rm ISW-tSZ} = \frac{C_\ell^{\rm ISW-tSZ}}{\sqrt{C_\ell^{\rm ISW} C_\ell^{\rm tSZ1h+2h}}}. \quad (27)$$

This can be easily understood since the tSZ one-halo term, as opposed to the two-halo term, does not trace the large-scale correlations and behaves as noise for the ISW–tSZ detection.

We then determine what would be the S/N that could be obtained for different redshift cut thresholds. Fig. 8 shows that the maximum S/N for the ISW–tSZ cross-correlation is reached when masking $z < 0.3$ clusters. A simple cut to mask low z clusters allows us to increase the S/N from 2.2 to 5.1. Should one also mask $M > 5 \times 10^{14}\,{\rm M}_\odot$ clusters only, the significance level would rise to $\sim 6\sigma$. These detection levels compare well with the results of Crittenden & Turok (1996), who found in their pioneering work that the expected S/N of a cross-correlation between CMB and an ideal survey that traces the matter distribution without redshift limitation is of the order of 5.5–7.4, depending on Ω_Λ value. Our results are also comparable with those obtained by Afshordi (2004), who claims that a detection at the level of $\sim 7.5\sigma$ for an ideal ISW–galaxy correlation should be expected. According to this work, this S/N is expected to be of the order of 5 for an all-sky survey with 10 million galaxies within $0 < z < 1$, provided the redshift systematic errors are lower than 0.05 and the systematic anisotropies of the survey do not exceed 0.1 per cent. Douspis et al. (2008) showed that a *Euclid*-like mission should ideally provide a detection of the ISW at a significance level of 5σ. Note that we obtain similar S/N with our approach but without the need to use non-CMB data.

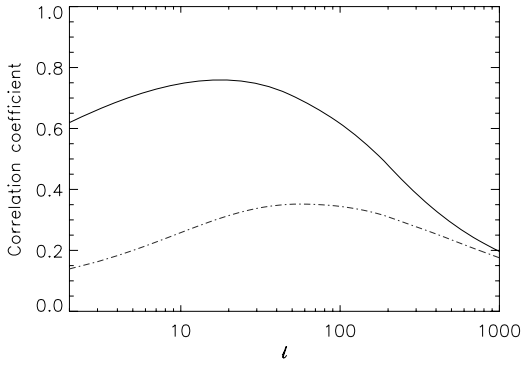

Figure 7. ISW–tSZ correlation coefficient. The solid black line is the coefficient after masking $z < 0.3$ clusters, which drastically reduces the tSZ one-halo term at multipoles lower than 100. The dot–dashed blue line is the correlation coefficient without any mask.

4.2 A more realistic approach: using a SZ selection function

The previously introduced sharp cuts in redshift assumed that redshifts and masses were available for a relevant subset of clusters. We now relax this assumption and build a theoretical selection function in order to determine which clusters can be detected – and thus masked – in a *Planck*-like survey.

A galaxy cluster is assumed to be detected through its SZ signal if its beam convolved Compton parameter exceeds the confusion noise and its integrated signal Y is higher than λ times the instrumental sensitivity simultaneously in the 100, 143 and 353 GHz channels, with λ the detection significance level (Bartelmann 2001; Taburet et al. 2009). The selection functions for 1σ, 3σ and 5σ detections are represented in Fig. 9.

As shown in Fig. 10, masking the clusters detected with a high detection significance (5σ, red line) increases the cumulative S/N to 3.7. When masking clusters that are detected at a 3σ level, the

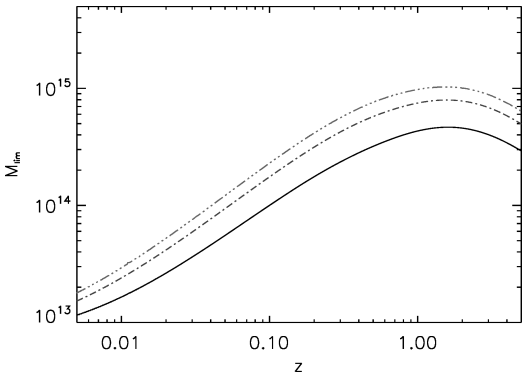

Figure 9. Selection functions for 1 (black solid line), 3 (dot–dashed blue line) and 5 (triple-dot–dashed red line) σ detection of SZ clusters for a *Planck*-like survey.

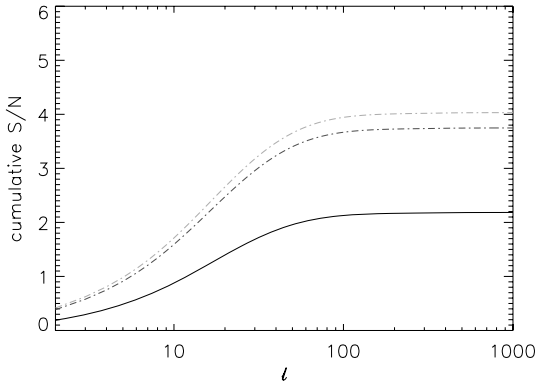

Figure 10. Cumulative S/N of the ISW–tSZ detection after masking the 5σ (dot–dashed red line) and 3σ (dot–dashed green line) detected SZ clusters. Black line reminds the result without masking any cluster.

cumulative S/N is enhanced to 4. Reaching this level of detection requires to mask faint clusters and thus suppose a good understanding of the cluster selection function.

5 IMPACT OF POINT SOURCES AND GALACTIC RESIDUALS

In the previous section we considered an idealized scenario in which the only signals were the primary CMB, the ISW, the tSZ and the instrumental noise. Nevertheless, it is of common knowledge that radio and infrared (IR) galaxies as well as our Galaxy are important contributors to the observed signal at submillimetre wavelengths. For that, we use state-of-the-art models describing the emission of the Milky Way and millimetre wavelengths, together with the contribution from radio and submillimetre sources. The frequencies for which we built our foreground model are 100, 143, 217 and 353 GHz, which correspond to the High Frequency Instrument (HFI) of the *Planck* mission.[2] We considered five different contaminants, namely free–free, synchrotron and dust emission (coming from our Galaxy), and radio and IR extragalactic sources. For the free–free and synchrotron, we scaled the maps produced by the *WMAP* team at the *V* and *W* bands of this experiment (corresponding to 74 and 94 GHz, respectively) to higher frequencies. We used the maps available at the LAMBDA repository,[3] and computed the effective spectral index in thermodynamic temperature for each pixel between the *V* and the *W* bands. These spectral indexes were used to extrapolate the thermodynamic temperature to the higher frequencies under consideration. The dust emission induced by the Milky Way was predicted in our frequency range by means of model 8 of Finkbeiner, Davis & Schlegel (1999, hereafter denoted by FDS).[4] This model predicts the galactic dust emission down to angular scales of $\sim$5 arcmin, which suffices in the context of ISW studies. Finally, we used the point-source maps produced by Sehgal et al. (2010), who modelled the contribution of the extragalactic source population, both in the radio and the submillimetre. In that work, a halo catalogue resulting from a large cosmological hydrodynamical simulation was populated with radio and dusty galaxies, in such a way that the spatial distribution of those sources follows the clustering of dark matter haloes. Both galaxy populations were designed to meet different constraints obtained from radio, IR and millimetre observations (see Sehgal et al. 2010 for details). They were projected on high resolution sky maps at different observing frequencies, which differ from HFI channels' central frequencies for a few per cent in most of the cases.

Our proposed approach to unveil the ISW–tSZ correlation compares CMB observations obtained at frequencies for which the tSZ is non-zero with CMB observations observed at 217 GHz. This frequency lies in the Wien region of the CMB blackbody spectrum, in which the CMB brightness drops very rapidly for increasing frequencies and dust contribution (both galactic and extragalactic) becomes dominant. Therefore, in a relatively narrow frequency range the CMB is surpassed by dust emission, and it is in this frequency range where an extrapolation of dust properties (observed at high frequencies) down to lower frequencies (where CMB is dominant) must be carried out. On the large angular scales of relevance for the ISW, the dust in the Milky Way is the main source of contamination, and its accurate subtraction is actually critical for our purposes. An experiment like HFI counts with frequency channels centred at 353, 545 and 857 GHz, which probe the regime where dust emission is well above the CMB contribution. We shall use those channels to correct for dust (both galactic and extragalactic) at lower frequencies. Our approach attempts by no means to be exhaustive or systematic, but simply tries to display the degree of accuracy required at subtracting dust emission in order to unveil the tSZ–ISW cross-correlation in a *Planck*-like experiment.

We first built a mask that covered those regions where the Milky Way emission, *both* in radio and submillimetre, was stronger. We sorted in intensity (from bigger to smaller values) the templates of free–free and synchrotron in the *V* band (as produced by the *WMAP* team) and the FDS dust template at 353 GHz. Masking a given level of emission (for instance, the 25 per cent of brightest pixels) in each template yielded two masks that were very similar (particularly in the galactic plane), with differences corresponding mostly to high latitude clouds being bright either in the radio or submillimetre (but not on both). The final mask was the product of the two masks built upon the radio and dust templates. The fraction of uncovered sky, $f_{\rm sky}$, was then set as a free parameter in the mask construction.

According to the FDS dust templates, one has to take into account the spatial variation of the effective spectral index if one is to accurately correct for dust emission in the 100–217 GHz frequency range. In these templates, an effective spectral coefficient in thermodynamic temperature (defined as the ratio of thermodynamic temperatures between two different channels, i.e. $\alpha_{353,j} \equiv \delta T_j/\delta T_{353\,\rm GHz}$) is correlated with the thermodynamic temperature at 353 GHz, as the left-hand panel of Fig. 11 shows. The curvature at low temperatures is a consequence of the grey body law describing the dust emission in IR galaxies, and we make use of it when subtracting the dust emission at low frequencies. In this low temperature regime, the effective spectral coefficients from IR galaxies differ from that of the Milky Way, and for this reason a more accurate scaling could be obtained by treating the local cirrus component separately from the extragalactic IR one. This can be achieved, in high latitude regions, using H1 data that trace the galactic cirrus emission, in order to remove their contribution. We sorted pixels of HEALPIX[5] (Górski et al. 2005) resolution parameter $N_{\rm side} = 64$ outside the mask according to their intensity in the dust template at 353 GHz, and binned them in groups of length $n_{\rm groups}$, in each of which a different estimate of $\alpha_{353,j}$ is estimated in the

[2] http://www.planck.fr/heading1.html.
[3] http://lambda.gsfc.nasa.gov.
[4] The data and the software to build this galactic dust map were downloaded from http://www.astro.princeton.edu/∼schlegel/dust/cmb/cmb.html.
[5] http://www.healpix.org.

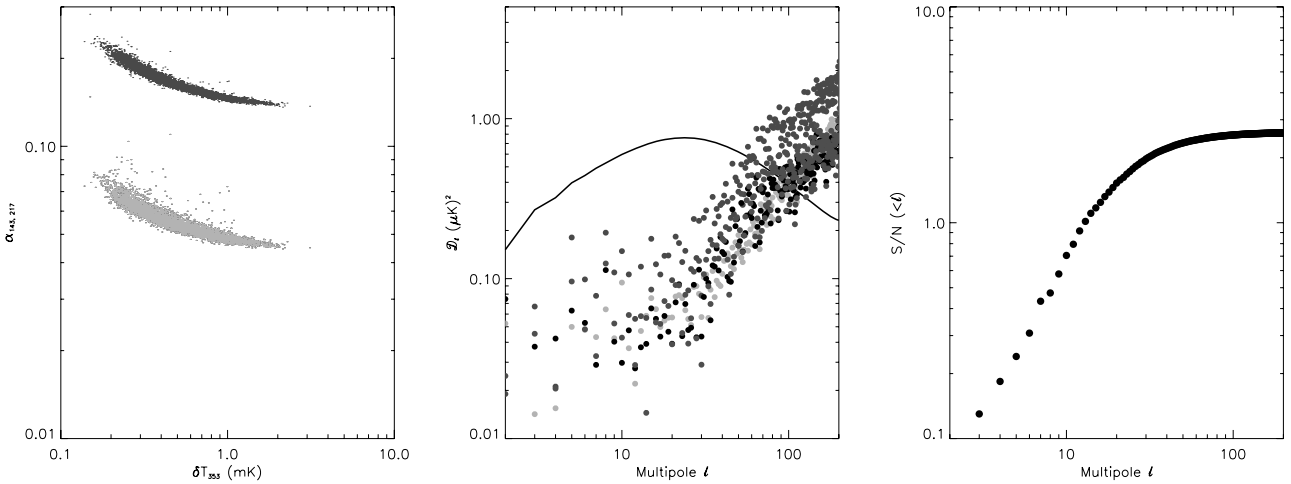

Figure 11. Left-hand panel: effective spectral coefficient between 353 GHz, on one hand, 143 GHz (green points) and 217 GHz (blue points). Middle panel: the expected ISW–tSZ cross-power spectrum amplitude (at 143 GHz, after masking all clusters below $z < 0.3$) given by the solid black line is compared to the residuals present in the 143 GHz (green circles) and 217 GHz (blue circles) channels, respectively. The effective bias in the ISW–tSZ cross-spectra are displayed by red circles, while the black ones display the increase in the error budget (last term in equation 34). Units are expressed in $\mathcal{D}_l \equiv l(l+1)C_l/(2\pi)$. Right-hand panel: cumulative S/N of the ISW–galaxy cross-power spectrum below a given multipole l.

low-frequency channels.[6] At these frequencies the observed signal in pixel $\hat{\boldsymbol{n}}$ is modelled as

$$T^j(\hat{\boldsymbol{n}}) = N^j(\hat{\boldsymbol{n}}) + \alpha_{353,\,j}(\hat{\boldsymbol{n}})M^{353}(\hat{\boldsymbol{n}}) + R^j(\hat{\boldsymbol{n}}), \tag{28}$$

where $M^{353}(\hat{\boldsymbol{n}})$ is the dust template at 353 GHz (including both galactic and extragalactic emission), $R^j(\hat{\boldsymbol{n}})$ is the extrapolation from the radio template of *WMAP*'s *V* band, and $N^j(\hat{\boldsymbol{n}})$ is what we regard as the noise component at frequency j. Most component separation algorithms attempt to fit for all relevant components (including CMB, radio and dust contributions) at each frequency. Now we concern only about the impact of dust residuals, which at these frequencies are dominant. We find however that by using a mask acting on the 10 per cent brightest pixels in the synchrotron plus free–free template, the effect of radio remains always below that due to dust. The effective noise N^j contains the residuals of a first-order CMB subtraction, and will be assumed to show no spatial correlations (i.e. to be white noise). For a high level of effective noise it will be necessary to bin the signal in larger groups (bigger $n_{\rm groups}$) in order to measure an average $\alpha_{353,j}$ throughout the bin. However, this average estimate of the effective spectral coefficient in the bin will produce an estimate of the dust contribution at frequency j and pixel $\hat{\boldsymbol{n}}$ that will *not correspond exactly* to the exact value, and this mismatch will be more relevant the wider the bins are (i.e. the bigger $n_{\rm groups}$ is). On the other hand, if noise were negligible one could make $n_{\rm groups} = 1$ and measure the dust contribution very accurately at each sky position $\hat{\boldsymbol{n}}$.

The residuals from the dust subtraction can be then written as

$$\delta T^j_{\rm res}(\hat{\boldsymbol{n}}) = T^j(\hat{\boldsymbol{n}}) - \tilde{\alpha}_{353,\,j} M^{353}(\hat{\boldsymbol{n}}), \tag{29}$$

where the $\tilde{\alpha}_{353,\,j}$ estimate is computed after minimizing

$$\chi^2 = \sum_{i,l} (T^j - \tilde{\alpha}_{353,\,j} M^{353})_i \mathbf{N}^{-1}_{i,l} (T^j - \tilde{\alpha}_{353,\,j} M^{353})_l, \tag{30}$$

and the indexes i and l are running from 1, $n_{\rm groups}$ in the bin to which the pixel $\hat{\boldsymbol{n}}$ belongs. The matrix $\mathbf{N}^{-1}$ corresponds to the noise inverse covariance matrix, which is diagonal if N is Poissonian noise. The estimate and error associated to $\tilde{\alpha_{353,\,j}}$ are given by

$$\tilde{\alpha}_{353,\,j} = \frac{\sum_{i,l} T^j_i \mathbf{N}^{-1}_{i,l} M^{353}_l}{\sum_{i,l} M^{353}_i \mathbf{N}^{-1}_{i,l} M^{353}_l}, \tag{31}$$

$$\sigma^2_{\tilde{\alpha}_{353,\,j}} = \frac{1}{\sum_{i,l} M^{353}_i \mathbf{N}^{-1}_{i,l} M^{353}_l}. \tag{32}$$

The residuals given by equation (29) will bias the tSZ–ISW correlation estimates, and also increase their errors. The former is given by the second term in right-hand side of this equation:

$$E\left[\left\langle \left(a^j_{l,m} - a^{217}_{l,m}\right)\left(a^{217}_{l,m}\right)^*\right\rangle\right] = C_l^{\rm ISW-tSZ_j} + \left\langle \left(a^{j,\,\rm res}_{l,m} - a^{217,\,\rm res}_{l,m}\right)\left(a^{217,\,\rm res}_{l,m}\right)^*\right\rangle, \tag{33}$$

where the multipoles of the residuals at channel j (equation 29) are given by the $a^{j,\,\rm res}_{l,m}$ values. The impact of residuals on the dispersion of the tSZ–ISW correlation estimates is modelled as in equation (24):

$$\Delta\left[C_l^{\rm ISW-tSZ_j}\right] = \left(C_l^{\rm ISW-tSZ_j}\right)^2 + C_l^{\rm CMB}\left(C_l^{{\rm tSZ_j},\,\rm 1h} + C_l^{{\rm tSZ_j},\,\rm 2h} + C_l^{j-217,\,\rm res}\right), \tag{34}$$

with $C_l^{j-217,\,\rm res}$ the power spectrum multipole of the residual difference map $\delta T^{\rm j}_{\rm res} - \delta T^{217}_{\rm res}$ and where we have assumed that the power spectrum of residuals at 217 GHz is much smaller than the CMB power spectrum ($C_l^{217,\,\rm res} \ll C_l^{\rm CMB}$). As before, the S/N for a given multipole will be given by $({\rm S/N})^2_l = (C_l^{\rm ISW-tSZ_j})^2/\Delta[C_l^{\rm ISW-tSZ_j}]$.

We computed the total S/N for the ISW–tSZ cross-correlation for different levels of sky coverage $f_{\rm sky}$, bin size $n_{\rm groups}$ and Gaussian white noise amplitude $\sigma_N \equiv \sqrt{\langle N_{ii}\rangle}$. We considered the case where all clusters below $z < 0.3$ are masked out, since it is the one giving rise to highest S/N in the ideal (contamination free) case, and a low frequency of 143 GHz. We first assumed a noise amplitude of $\sigma_N = 80\,\mu$K in square pixels of 5 arcmin size, and checked for the resulting S/N after binning in groups of varying length $n_{\rm groups}$. This noise amplitude is above the predicted values for HFI channels 100, 143 and 217 GHz, for which values of 14.2, 9 and 14.6 μK in pixels of size 5 arcmin are expected. One would

[6] Unless otherwise specified, this is the pixelization resolution used in our analyses.

guess, however, that any component separation algorithm (required to remove an estimation of the CMB in each channel) would sensibly increase the overall noise level. We found that after binning pixels in groups of size $n_{\rm groups} = 1000$ and masking 40 per cent of the sky, residuals would drop below the ISW–tSZ cross-correlation amplitude for the 143 and 217 GHz channels. In the middle panel of Fig. 11 green circles display the amplitude of dust residuals at 143 GHz, while those at 217 GHz are given by blue circles. The effective bias on the ISW–tSZ cross-correlation (which is given by the solid thick line) are shown by red circles. The extra (last) term in the error computed in equation (34) is displayed by black circles. In all cases we are showing *pseudo*-power spectrum multipoles. In this configuration, the total S/N achieved was approximately 2.6 (as shown by the right-hand panel of Fig. 11). When comparing to fig. 6 of Leach et al. (2008), we see that our level of residuals is comparable to those obtained after using the whole set of *Planck* frequencies for component separation. The accuracy of our simple cleaning procedure is displayed by Fig. 12: the top panel shows the total contaminant emission at 217 GHz, while the bottom one displays the residuals after the cleaning procedure described above was applied. We repeated this analysis but after considering the not-so-optimistic scenario of Fig. 10, where we use an approximation for *Planck* cluster detection window function. More precisely, we adopted the model for which all clusters detected at 5σ were removed. In this case, the S/N drops from $\sim$3.7 in the ideal (foreground free) case down to $\sim$1.46. According to this result, it seems that relying exclusively on *Planck*'s ability to detect nearby clusters and remove them will not yield sufficient S/N: it becomes necessary to use external galaxy cluster catalogues [such as e.g. the Meta Catalogue of X-ray detected Clusters (MCXC), Piffaretti et al. 2011] to perform a more accurate subtraction of the nearby tSZ signal.

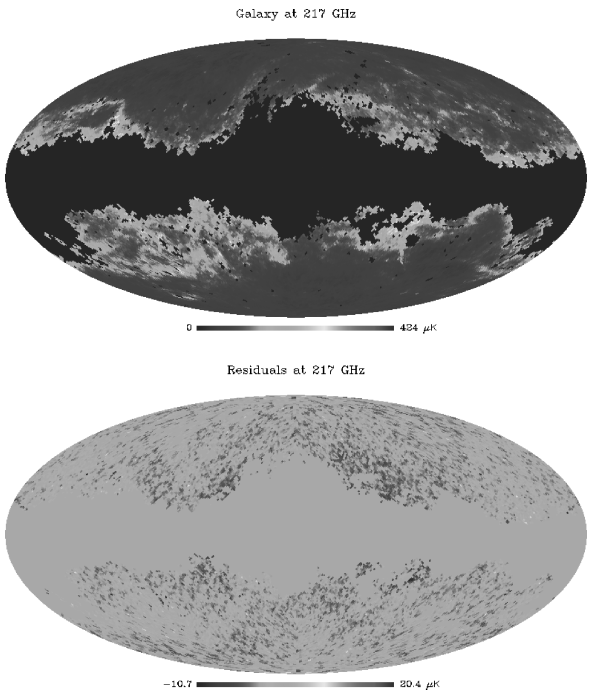

Figure 12. Top panel: total galactic emission outside the mask covering 40 per cent of the sky at 217 GHz in thermodynamic temperature units. Bottom panel: residuals outside the mask at 217 GHz after using a perfect dust tracer at 353 GHz and assuming a white noise level of 80 μK at scales of 5 arcmin.

We also explored how S/N depends on σ_N and $n_{\rm groups}$, see Fig. 13. The top panel shows how S/N varies with σ_N for different values of $n_{\rm groups}$: black, red, green and blue lines correspond to $n_{\rm groups} =$ 1, 10, 100 and 1000, respectively. In the bottom panel, those same colours correspond to $\sigma_N = 1$, 10, 50 and 100 μK, respectively. The top panel displays how S/N is degraded as the noise level is increased, being this degradation more important for low values of $n_{\rm groups}$ for the same value of σ_N. However, in the cases of low noise, the reconstruction of dust is more accurate for small $n_{\rm groups}$ and higher values of S/N are reached in such cases. The bottom panel, instead, shows how increasing the bin width ($n_{\rm groups}$) improves the S/N only in the regime where noise is dominating: for low noise levels binning only degrades the quality of the subtraction. Note that in ideal conditions ($n_{\rm groups} = 1$, $\sigma_N = 0$ μK), S/N $\simeq 3.9$ for $f_{\rm sky} =$ 0.6 considered here.

6 DISCUSSION AND CONCLUSIONS

The problem of component separation in multifrequency CMB observations for experiments like *Planck* has been a subject of active investigation (e.g. Stolyarov et al. 2005; Aumont & Macías-Pérez

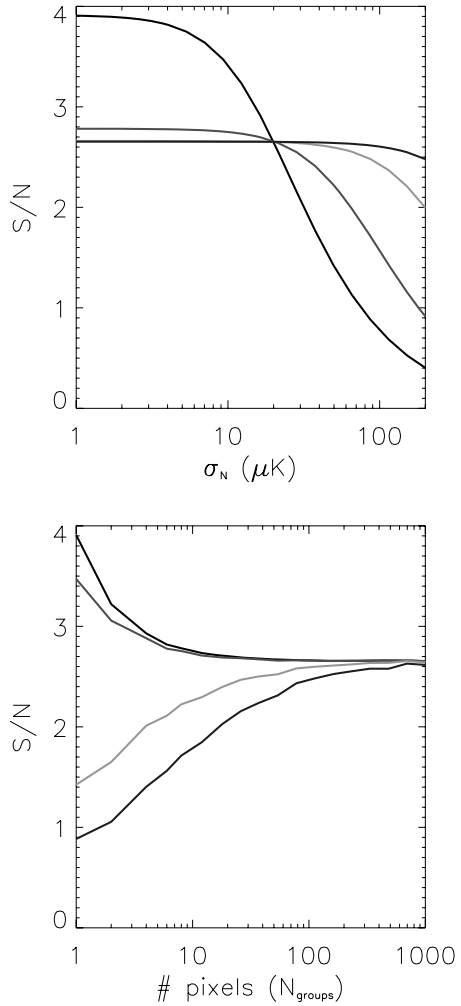

Figure 13. Top panel: S/N versus residual effective noise for different values of $n_{\rm groups}$: black, red, green and blue lines correspond to $n_{\rm groups} = 1$, 10, 100 and 1000, respectively. Bottom panel: S/N versus bin width $n_{\rm groups}$: black, red, green and blue lines correspond to $\sigma_N = 1$, 10, 50 and 100 μK, respectively.

2007; Eriksen et al. 2008; Leach et al. 2008; Stompor et al. 2009). The different contaminants (either galactic or extragalactic) show generally a different spectral dependence when compared to the CMB. On the low-frequency side, foreground powerful in radio wavelengths fall steeply and become the subdominant foregrounds at frequencies above $\nu \sim 70$ GHz (Bennett et al. 2003). Above this frequency, the presence of dust absorbing ultraviolet radiation and re-emitting it in the submillimetre and millimetre range constitutes the dominant contaminant. An experiment like *Planck*, with four high angular resolution channels covering the 217–857 GHz frequency range, should provide an accurate description of this foreground. With these data in hand, currently existing models describing the physics of dust emission should be improved further and accurate extrapolations to lower frequencies should be enabled.

In our toy model describing the impact of the contaminants we assumed that the 353 GHz channel was a perfect (CMB-free) dust tracer, and that the signal at low frequencies (100 or 143 GHz) was either due to dust or a white Gaussian noise signal. These assumptions may be overly optimistic (in regard to the 100 and 217 GHz channels themselves), but however a generic combination of all nine channels (ranging from 30 to 857 GHz) are expected to provide an estimation of each of the components (CMB + foregrounds) whose residuals are expected to lie close to the level of $\sim$0.1 $(\mu\mathrm{K})^2$ (Leach et al. 2008). This is already the accuracy ballpark that our simple analysis proved to define the regime of detectability of the tSZ–ISW cross-correlation, and there may still be room for a more optimized channel combination oriented to unveil the particular tSZ–ISW cross-correlation. The use of high galactic latitude H I maps as tracers of galactic cirrus could allow us to lower the impact of those residuals at the level of a percent in C_ℓ (Lagache, private communication). Fernandez-Conde et al. (2008) computed the cirrus power spectrum at different frequencies and different H I column densities. They found, in the case of fields that have a very low level of dust contamination, that the cirrus power spectrum at 217 GHz is of the order of 5 $(\mu\mathrm{K_{RJ}})^2$ at $\ell = 10$ in units of $l(l+1)C_l/(2\pi)$. A one percent residual of the cirrus emission is thus smaller than 0.05 $(\mu\mathrm{K_{RJ}})^2$, i.e. 0.4 $(\mu\mathrm{K_{CMB}})^2$. Current foreground residual estimates based upon the works of Fernandez-Conde et al. (2008) and Leach et al. (2008) suggest that at the frequencies of interest (100–217 GHz) the contaminant residuals remain a factor of a few above our requirements. How much room there is for improvement below those limits is something yet to be estimated from real data.

Planck data at high frequencies provide a more profound knowledge of the dust properties in both our Galaxy and extragalactic sources, together with the mechanisms involving its emission in the submillimetre range. It is nevertheless important to bear in mind that, since the different frequencies sample the IR galaxy populations at different redshifts and the galaxy linear bias evolves with redshift (e.g. Lagache et al. 2007; Viero et al. 2009), using high-frequency maps so as to clean the 143 and 217 GHz could potentially degrade the residual level we obtained in Section 5 with our template fitting method. This issue is under current investigation within the *Planck* collaboration.

Even in the worst scenario in which foreground residuals are too high and complicated to prevent the detection of the tSZ–ISW cross-correlation, the upper limits to be imposed on it are of cosmological relevance, since it would constrain cosmological parameters like σ_8, Ω_m or Ω_Λ.

We have shown that the tSZ–ISW cross-correlation constitutes a CMB contained test for dark energy. The peculiar frequency dependence of the tSZ effect and the availability of multifrequency all-sky CMB observations provided by the experiment *Planck* should enable an estimation of this cross-correlation provided the hot gas is a fair tracer of the potential wells during the cosmological epochs where the ISW is active. Our theoretical study shows that the Poisson/shot noise introduced by the modest number of very massive, very bright in tSZ galaxy clusters can be attenuated by masking out those tSZ sources below redshift $z < 0.3$. In the absence of a massive galaxy cluster catalogue below that redshift, it would suffice to excise from the analysis those tSZ clusters clearly detected by *Planck* in order to achieve S/N of the order of 3.9 ($f_\mathrm{sky} = 1$). This scenario however seems to be more affected by foreground residuals, so aid from an external cluster catalogue like MCXC might be required. Therefore, this tSZ–ISW cross-correlation detection would not require the use of deep-in-redshift and wide-in-angle galaxy surveys, but only the combination of different frequency CMB observations plus occasionally (existing) external cluster catalogues. This would hence provide a different approach for ISW detection with different systematics to other attempts based upon CMB–galaxy survey cross-correlations. If foreground residuals are kept at or below the $\sim$0.04 $(\mu\mathrm{K})^2$ level [in $l(l+1)C_l/(2\pi)$ units at $l \sim 10$] in the frequency range 100–217 GHz, then the tSZ–ISW correlation should provide a valid and independent test for the impact of dark energy on the growth of structure and the evolution of large angle CMB temperature anisotropies.

ACKNOWLEDGMENTS

NT is grateful for hospitality from the Max-Planck-Institut für Astrophysik in Garching where part of this work was done. NT warmly thanks Guilaine Lagache, Aurélie Penin and Mathieu Langer for useful discussions that helped improving this paper. CH-M is also grateful to the Institut d'Astrophysique Spatiale (IAS) for its warm hospitality during his frequent visits to Orsay.

REFERENCES

Afshordi N., 2004, Phys. Rev. D, 70, 083536
Afshordi N., Loh Y., Strauss M. A., 2004, Phys. Rev. D, 69, 083524
Aghanim N., Majumdar S., Silk J., 2008, Rep. Prog. Phys., 71, 066902
Arnaud M., Pratt G. W., Piffaretti R., Boehringer H., Croston J. H., Pointecouteau E., 2010, A&A, 517, 92
Aumont J., Macías-Pérez J. F., 2007, MNRAS, 376, 739
Bartelmann M., 2001, A&A, 370, 754
Battye R. A., Weller J., 2003, Phys. Rev. D, 68, 083506
Bennett C. L. et al., 2003, ApJS, 148, 97
Bielby R., Shanks T., Sawangwit U., Croom S. M., Ross N. P., Wake D. A., 2010, MNRAS, 403, 1261
Boughn S. P., Crittenden R. G., 2004, Nat, 427, 45
Cabré A., Gaztañaga E., Manera M., Fosalba P., Castander F., 2006, MNRAS, 372, L23
Cole S., Kaiser N., 1988, MNRAS, 233, 637
Cooray A., 2002, Phys. Rev. D, 65, 103510
Cooray A., Sheth R., 2002, Phys. Rep., 372, 1
Crittenden R. G., Turok N., 1996, Phys. Rev. Lett., 76, 575
Douspis M., Castro P. G., Caprini C., Aghanim N., 2008, A&A, 485, 395
Dunkley J. et al., 2011, ApJ, 739, 52
Eriksen H. K., Jewell J. B., Dickinson C., Banday A. J., Górski K. M., Lawrence C. R., 2008, ApJ, 676, 10
Fernandez-Conde N., Lagache G., Puget J., Dole H., 2008, A&A, 481, 885
Finkbeiner D. P., Davis M., Schlegel D. J., 1999, ApJ, 524, 867 (FDS)
Fosalba P., Gaztañaga E., 2004, MNRAS, 350, L37
Fosalba P., Gaztañaga E., Castander F. J., 2003, ApJ, 597, L89
Giannantonio T. et al., 2006, Phys. Rev. D, 74, 063520

Giannantonio T., Scranton R., Crittenden R., Nichol R. C., Boughn S. P., Myers A. D., Richards G. T., 2008, Phys. Rev. D, 77, 123520
Górski K. M., Hivon E., Banday A. J., Wandelt B. D., Hansen F. K., Reinecke M., Bartelmann M., 2005, ApJ, 622, 759
Granett B. R., Neyrinck M. C., Szapudi I., 2008, ApJ, 683, L99
Granett B. R., Neyrinck M. C., Szapudi I., 2009, ApJ, 701, 414
Hernández-Monteagudo C., 2008, A&A, 490, 15
Hernandez-Monteagudo C., 2010, A&A, 520, 101
Hernández-Monteagudo C., Sunyaev R. A., 2005, MNRAS, 359, 597
Hernández-Monteagudo C., Génova-Santos R., Atrio-Barandela F., 2006a, in Mornas L., Diaz Alonso J., eds, AIP Conf. Ser. Vol. 841, A Century of Relativity Physics: ERE 2005. Am. Inst. Phys., New York, p. 389
Hernández-Monteagudo C., Verde L., Jimenez R., Spergel D. N., 2006b, ApJ, 643, 598
Ho S., Hirata C., Padmanabhan N., Seljak U., Bahcall N., 2008, Phys. Rev. D, 78, 043519
Komatsu E., Kitayama T., 1999, ApJ, 526, L1
Komatsu E., Seljak U., 2002, MNRAS, 336, 1256 (KS02)
Komatsu E. et al., 2009, ApJS, 180, 330
Komatsu E. et al., 2011, ApJS, 192, 18
Lagache G., Bavouzet N., Fernandez-Conde N., Ponthieu N., Rodet T., Dole H., Miville-Deschênes M.-A., Puget J.-L., 2007, ApJ, 665, L89
Leach S. M. et al., 2008, A&A, 491, 597
López-Corredoira M., Sylos Labini F., Betancort-Rijo J., 2010, A&A, 513, A3
Loverde M., Afshordi N., 2008, Phys. Rev. D, 78, 123506
Lueker M. et al., 2010, ApJ, 719, 1045
Martinez-Gonzalez E., Sanz J. L., Silk J., 1990, ApJ, 355, L5
McEwen J. D., Vielva P., Hobson M. P., Martínez-González E., Lasenby A. N., 2007, MNRAS, 376, 1211
Mo H. J., White S. D. M., 1996, MNRAS, 282, 347
Negrello M., Magliocchetti M., De Zotti G., 2006, MNRAS, 368, 935
Nolta M. R. et al., 2004, ApJ, 608, 10
Padmanabhan N., Hirata C. M., Seljak U., Schlegel D. J., Brinkmann J., Schneider D. P., 2005, Phys. Rev. D, 72, 043525
Pietrobon D., Balbi A., Marinucci D., 2006, Phys. Rev. D, 74, 043524
Piffaretti R., Arnaud M., Pratt G. W., Pointecouteau E., Melin J., 2011, A&A, 534, 109
Raccanelli A., Bonaldi A., Negrello M., Matarrese S., Tormen G., de Zotti G., 2008, MNRAS, 386, 2161
Rassat A., Land K., Lahav O., Abdalla F. B., 2007, MNRAS, 377, 1085
Sachs R. K., Wolfe A. M., 1967, ApJ, 147, 73
Sawangwit U., Shanks T., Cannon R. D., Croom S. M., Ross N. P., Wake D. A., 2010, MNRAS, 402, 2228
Scranton R. et al., 2003, arXiv:astro-ph/0307335
Sehgal N. et al., 2010, ApJ, 709, 920
Shaw L. D., Nagai D., Bhattacharya S., Lau E. T., 2010, ApJ, 725, 1452
Sheth R. K., Mo H. J., Tormen G., 2001, MNRAS, 323, 1
Stolyarov V., Hobson M. P., Lasenby A. N., Barreiro R. B., 2005, MNRAS, 357, 145
Stompor R., Leach S., Stivoli F., Baccigalupi C., 2009, MNRAS, 392, 216
Sunyaev R. A., Zel'dovich Y. B., 1972, Comments Astrophys. Space Phys., 4, 173
Taburet N., Aghanim N., Douspis M., Langer M., 2009, MNRAS, 392, 1153
Vielva P., Martínez-González E., Tucci M., 2006, MNRAS, 365, 891
Viero M. P. et al., 2009, ApJ, 707, 1766
Vikhlinin A. et al., 2009, ApJ, 692, 1060

This paper has been typeset from a TEX/LATEX file prepared by the author.